Received: March 14, 2023. Revised: April 23, 2023.

International Journal of
Intelligent Engineering & Systems

http://www.inass.org/

Optimal Deep Learning Based Atherosclerotic Plaque Classification on Intravascular Ultrasound Images

Nisha K. Prajapati[1]* **Amit V. Patel[1]**

[1]*V. T. Patel Department of Electronics & Communication Engineering, Chandubhai S. Patel Institute of Engineering, Charotar University of Science and Technology, Charusat Campus, Changa, India*
* Corresponding author's Email: 20drec002@charusat.edu.in

Abstract: Intravascular ultrasound (IVUS) is suitable for evaluating plaque and lesion morphology features and helps to make clinical decisions during the treatment of coronary artery disease (CAD). IVUS remain a gold standard in accessing atherosclerosis plaques, coronary lesions, and stenosis. Even though plaque classification by IVUS is essential for risk stratification, frame-by-frame analysis of an entire vascular segment is labor intensive. In recent times, in the field of deep learning (DL), convolutional neural network (CNN) has been intended to adaptively and automatically determine the spatial hierarchy through backpropagation. The study develops an optimal deep transfer learning based on atherosclerotic plaque and calcification on intravascular ultrasound images (ODTL-APCIUI) technique. The presented ODTL-APCIUI technique aims to classify atherosclerotic plaque and calcification. To accomplish this, the presented ODTL-APCIUI technique preprocesses the IVUS images by Gaussian filtering (GF) technique. In addition, U2Net model is applied for the segmentation process with Adam optimizer based hyperparameter tuning. Moreover, the ODTL-APCIUI technique uses DenseNet-169 model for feature extraction purposes. Furthermore, the ODTL-APCIUI technique exploits stacked autoencoder (SAE) for classification process. Finally, Harris Hawks optimization (HHO) algorithm is exploited for the hyperparameter adjustment of the SAE approach. The performance assessment of ODTL-APCIUI algorithm is tested using medical images and the results are investigated under different metrics. The experimental outcomes demonstrated that the ODTL-APCIUI technique has gained better performance with maximum accuracy of 97.19%, precision of 94.09%, sensitivity of 97.17%, specificity of 97.19%, and F-score of 92.52%.

Keywords: Intravascular ultrasound images, Atherosclerotic plaque detection, Convolution neural network, Deep learning, Harris hawks optimization.

1. Introduction

Diabetes, smoking, and hypertension are amongst the main risk factor for atherosclerosis which is the major reason for cardiovascular disease (CVD). Atherosclerosis is the progress of cholesterol, fats, and other forms and substances through a slower progression. After a while, this plaque narrows the luminal regions and thickens the walls of arteries [1]. Hence, intracoronary imaging of vessel wall architecture is critical to assess plaque regression or progression during prognosis, diagnosis, and treatment [2]. Intravascular ultrasound (IVUS) and coronary angiography are conventional imaging modalities for CVD diagnoses. Angiography is the more common approach for intracoronary imaging through catheterization and is implemented alongside X-ray analysis which provides data on the luminal size of arteries [3]. IVUS is a helpful assistant to angiography since it gives pathological and morphological real time data on plaque and artery wall [4]. Plaque burden is positioned between the luminal borders and media–adventitia in the vessel wall. Generally, the diagnosis of media–adventitia border is lesser challenging than luminal border since the media layer encompasses smooth cells demonstrated as a dark ring in IVUS image [5]. On the other hand, differentiating the intima layer is

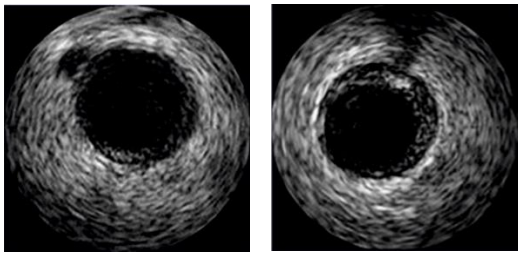

(a) (b)

Figure. 1 Sample IVUS image: (a) absence of calcification and (b) presence of calcification

somewhat challenging due to great scattering from erythrocytes within the lumen. Thus, automated estimate of the luminal borders and media–adventitia is indispensable to evaluate the degree of stenosis and luminal region during IVUS-assisted diagnoses [6]. Whereas many automatic solutions have been introduced for assisting IVUS segmentation, not any technique has demonstrated its potential to precisely identify the external elastic membrane (EEM) and lumen border and process IVUS images in real-time [7]. Fig. 1 shows the samples IVUS image.

Due to the popularization of imaging inspection and the ongoing progress of imaging technology, enormous image dataset has been produced [8]. In the meantime, big data is a major driver in the advancement of accuracy medicine researchers and clinicians alike have greater opportunity to engage in the evaluation and development of novel image analysis algorithm, with the final objective of generating new tools to enhance patient care [9]. Lately, artificial intelligence (AI) technology is considered a stimulating study topic in different areas, as considerable progress in AI has occurred. The application of AI enables the recognition of the data that enhances medical work efficacy. In addition, AI has been recently propelled towards the study of CVD imaging [10]. Deep learning (DL) methodology had already started to find medical applications in enabling the accurate and rapid processing of larger imaging datasets. They rely on learning from larger dataset of human annotation and utilize this data for training algorithmic model that can able to process images and replicate human performance within a second.

This study develops an optimal deep transfer learning based on atherosclerotic plaque and calcification on intravascular ultrasound images (ODTL-APCIUI) technique. The presented ODTL-APCIUI technique performs preprocessing using Gaussian filtering (GF) technique. Besides, U2Net model has applied for the segmentation process with Adam optimizer based hyperparameter tuning. In addition, the ODTL-APCIUI technique uses DenseNet-169 model for feature extraction purposes. Moreover, the ODTL-APCIUI technique exploits stacked autoencoder (SAE) for classification process. At the final stage, Harris hawks optimization (HHO) algorithm is exploited for the hyperparameter adjustment of the SAE approach. The performance assessment of the ODTL-APCIUI approach is tested using medical images and the results are examined under different metrics. In short, the paper contributions are summarized as follows.

- An intelligent ODTL-APCIUI technique comprising of pre-processing, Adam with U-Net segmentation, DenseNet-169 based feature extraction, SAE classification, and HHO based parameter tuning is presented. To the best of our knowledge, the ODTL-APCIUI model has never presented in the literature.
- A novel Adam optimizer with U-Net model is used for the segmentation of the pre-processed images.
- Hyperparameter optimization of the SAE model using HHO algorithm using cross-validation helps to boost the predictive outcome of the ODTL-APCIUI model for unseen data.

The rest of the paper is organized as follows. Section 2 provides the related works and section 3 offers the proposed model. Then, section 4 gives the result analysis and section 5 concludes the paper.

2. Related works

Bargsten et al. [11] scientifically examined distinct capsule network framework variants and enhanced the accuracy of the segmentation of IVUS images. Later, the capsule network is compared to convolutional neural network (CNN) under different quantities of network parameters and training images. Outcomes compared to prior studies, the capsule network implements better while doubling more than a few capsule types afterwards every downsampling phase, similar to typical increase rate of feature map in CNN. Bajaj et al. [12] validate and develop a DL method based on the IVUS image segmentation sequence in real-time. Validation of the presented method can be performed in twenty vessels through the approximation of two skilled experts as the reference standard. The proposed technique seems to be precise and can able to segment higher-resolution real-time IVUS datasets.

The authors in [13], proposed an end-to-end DL-CNN for automatically identifying luminal regions, calcified plaque and media–adventitia borders in IVUS images. A total of 713 grayscale images from

eighteen patients has been exploited as training dataset. In [14], developed an automatic system with the DL technique for detecting the calcification presence and absence in coronary artery IVUS images. An effective benefit of DL, compared to other techniques is, it applies features and representations directly from the raw information, bypassing the requirement to extract feature, a common that needed in the conventional machine learning (ML) architecture. The kind of DL framework utilized is twenty seven layers of CNN using direct acyclic graph.

Liu et al. [15] validated and developed an architecture for precise automatic quantification and detection of calcified plaque in coronary artery disease (CAD) as witnessed by IVUS. Calcified lesion was identified by training support vector classifiers for each IVUS A-line on annotated IVUS image, and post-processing using regional data. Then employed the architecture to thirty five IVUS pullbacks from all three widely applied IVUS systems. Cho et al. [16] developed an IVUS-based algorithm for categorizing calcified and attenuation plaque. The IVUS-based DL technique implemented accurate and fast calculation of the range of attenuated and calcified plaques in entire vessels. The data driven technique might help clinician easily recognize higher risk coronary lesion and makes treatment decision. Sofian et al. [17] presented an automatic DL system to identify the absence and presence of calcification in IVUS image. The traditional practice is for clinicians and radiologists to identify calcification through visual examination. The presented technique applied CNN, termed AlexNet, with six kinds of classifiers. In [18], a fully automated technique through an eight-layer U-Net is proposed for segmenting the area bounded by EEM and the coronary artery lumen. The dataset encompasses single-frequency and single-vendor IVUS information. Especially, the presented data augmentation of MeshGrid integrated with rotation and flip operations are performed which improve the efficiency.

Several CAD models are existed in the literature to perform atherosclerotic plaque and calcification process. Though several ML and DL models for atherosclerotic plaque and calcification are available in the literature, it is still needed to enhance the classification performance. Owing to continual deepening of the model, the number of parameters of DL models also increases quickly which results in model overfitting. At the same time, different hyperparameters have a significant impact on the efficiency of the CNN model. Particularly, the hyperparameters such as epoch count, batch size, and learning rate selection are essential to attain effectual outcome. Since the trial-and-error method for hyperparameter tuning is a tedious and erroneous process, metaheuristic algorithms can be applied. Therefore, in this work, we employ HHO algorithm for the parameter selection of the SAE model.

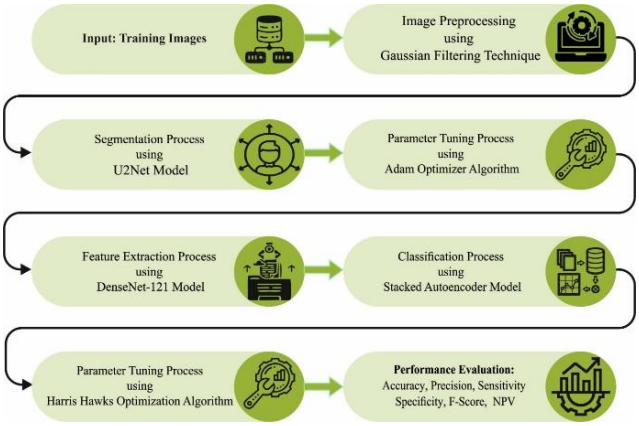

Figure. 2 Workflow of ODTL-APCIUI approach

3. The proposed model

In this study, we have developed a new ODTL-APCIUI technique for the classification of atherosclerotic plaque and calcification on the IVUS images. The presented ODTL-APCIUI technique encompasses GF based preprocessing, U-Net segmentation, DenseNet-169 feature extraction, SAE based classification, and HHO based hyperparameter tuning. The design of HHO algorithm helps in the proper election of the hyperparameters of the SAE classification model. Fig. 2 depicts the workflow of ODTL-APCIUI approach.

3.1 Image preprocessing using GF technique

In this study, the proposed technique uses GF to get rid of the noise exists in the IVUS images. The GF approach is used for image filtering process that removes the noise content and enhances the image quality [19]. A 2D GF technique is used to improve the quality of the dental system. The convolutional operation can be resolved using Gaussian function, and the Gaussian smoothing was attained by using the convolutional function. The Gaussian function in 1D can be formulated by Eq. (1):

$$G_{1D}(x) = \frac{1}{\sqrt{2\pi}\sigma} e^{-\left(\frac{x^2}{2\sigma^2}\right)} \quad (1)$$

The optimal smoothening filter of the image performs localization in the frequency and spatial

Table 1. Notations used

Notation	Meaning
$G_{1D}(x)$	1D Gaussian function
$G_{2D}(x,y)$	2D Gaussian function
(x,y)	Cartesian coordinates of image
σ	Standard deviation
g_t	Gradient
t	Time step
β_1, β_2	Exponential decay rate
α	Step size
L	Loss function
W_1	Weighted matrix of encoding function
f	Encoder function
b_1, b_2	Bias vector
g	Decoder function
W_2	Weighted matrix of decoding function
X_m	Average location of Hawks
E_0	Initial escaping energy
T	Maximum number of iterations
$\triangle X(n)$	Position vector of rabbits
u, v	Random values
E_0	First energy
X_{rabbit}	Rabbit location

domain while the ambiguity connection is satisfied as follows:

$$\Delta x \Delta \omega \geq \frac{1}{2} \tag{2}$$

The Gaussian operator in 2D is determined by the following expression:

$$G_{2D}(x,y) = \frac{1}{2\pi\sigma^2} e^{-\left(\frac{x^2+y^2}{2\sigma^2}\right)} \tag{3}$$

Where σ shows the standard deviation (SD) of Gaussian operator and (x,y) indicates the Cartesian coordinates of an image.

3.2 U2-Net segmentation

For image segmentation process, the U2-Net model is applied in this work. The U2-net is a two-stage nested U-architecture [20]. The outer layer is a larger U-architecture comprising eleven stages. All the stages are populated using a residual U-block (RSU) (inner layer). In theory, the nested U-architecture allows the extraction of multiscale and multilevel features more effectively. It comprises three parts: (1) map fusion module, (2) encoder, and (3) decoder given as follows:

- There are six phases in the encoder. All the stages are made up of RSU. In the RSU of the first 4 phases, the feature maps are decreased for increasing the receptive field and to attain more largescale data. In the following two phases, dilated convolution is applied for replacing the pooling function. This phase is essential for preventing contextual data loss. The receptive field is improved while the feature map is not decreased.
- The decoder stage has structure same as the encoder stage. All the decoder stages concatenate the up-sampled feature map from its preceding phase and symmetrical encoder phase as an input.
- Feature map fusion through a deep supervision approach is the final phase employed for generating the probability map. It generates six side outputs. Then, this output was up-sampled to the size of input images and combined with the concatenation function.

In summary, the U2-net architecture has lower memory and computing costs and deep architecture with rich multiscale features. Furthermore, as the U2-net structure is based on the RSU block and doesn't utilize pretrained backbone, it is easy and flexible to be adapted to working environment with low performance penalty.

Adam is the first order gradient based stochastic objective function optimization technique [21] which incorporates the benefit of RMSProp and AdaGrad techniques. To tune the optimal hyperparameter, the Adam optimizer is applied; the former is exploited for the sparse gradient problem, and the final one is applied for non-linear and unfixed optimization issues. Adam has the benefit of higher computing efficacy, low memory requirements, and easier implementation. It is gradient diagonal scaling is invariant, therefore it is applicable to resolve problems with largescale data or parameters. For dissimilar parameters, Adam upgrades the weight of NN and adaptively alters the learning rate based on training data. The computation procedure of Adam optimizer is demonstrated in Algorithm 1.

3.3 Feature extraction using DenseNet model

To generate a useful set of feature vectors, the DenseNet-169 model is exploited. DenseNet is the new expansion to neural network (NN) applied for detecting visual objects. The DenseNet169 is process of DenseNet group. The DenseNet group was proposed to implement image classification [22]. DenseNet169 is greater than other DenseNet groups. The DenseNet model is used for connecting all the layers in a feedforward manner. Generally, the standard convolutional network takes *L* layer. Furthermore, *L* connecting presents amongst *L* layer. That indicates one connection among all the layers

Algorithm 1: Pseudocode of Adam optimizer

g_t^2 represents the ce $(g_t \odot g_t)$. Default settings for the tested ML problem are $\alpha = 0.001, \beta_1 = 0.9, \beta_2 = 0.999, e = 10^{-8}$. All the operations on vector are element-wise. Using β_1^t and β_2^t we describe β_1 and β_2 to the power t:
Require: α: Step-size
Require: $\beta_1, \beta_2 \in [0,1)$: Exponential decay rate for the moment estimation
Require: (θ): Stochastic objective function with θ variable
Require: θ_0: Initial parameter vector
$m_0 \leftarrow 0$ (Initialize first moment vector)
$v_0 \leftarrow 0$ (Initialize second moment vector)
$t \leftarrow 0$ (Initialize timestep)
While θ_t not converged do

$$t \leftarrow t + 1$$

$g_t \leftarrow \nabla_\theta f_t(\theta_{t-1})$ (Get gradient wr.t. stochastic objective at t timestep)
$m_t \leftarrow \beta_1 \cdot m_{t-1} + (1 - \beta_1) \cdot g_t$ (Upgrade biased initial moment estimation)
$v_t \leftarrow \beta_2 \cdot v_{t-1} + (1 - \beta_2) \cdot g_t^2$ (Upgrade biased second raw moment estimation)
$mb_t \leftarrow m_t / (1 - \beta_1^t)$ (Evaluate bias-corrected 1st-moment estimation)
$vb_t \leftarrow v_t / (1 - \beta_2^t)$ (Evaluate bias-corrected 2nd-moment estimation)
$\theta_t \leftarrow \theta_{t-1} - a \cdot mb_t / (\sqrt{v} b_t + \varepsilon)$ (Upgrade variable)
End while
Return θ_t (Resulting variable)

and their succeeding layers. It attains L (L+1)/2 direct connection in the network. For all the layers as input, every presiding layer was exploited. For input of every succeeding layer, its feature maps are applied. It has several benefits in DenseNet. It decreases the gradient vanishing problems. The proposed framework has been assessed on competitive image recognition benchmark ImageNet and applied the load and store functions. The group of layers are defined if there is an entire similarity in the feature map dimensions at time of addition or concatenation. The batch normalization (BN) was performed by using downsampling with transition layer. The rate of development can be denoted as K.

$$k_l = k_0 + k \times (l - 1) \tag{4}$$

3.4 Image classification using SAE model

In this work, the SAE model is exploited for classification process. Auto-encoder (AE) is a kind of unsupervised learning mechanism which encompasses hidden, output, and input layers [23]. The process of AE training encompasses decoding and encoding functions. The encoding function maps the input dataset for hidden representation, and decoder reconstructs input dataset in the hidden depiction. Given that the unlabelled input dataset $\{x_n\}_{n=1}^N$, whereby $x_n \in R^{m \times 1}$, h_n shows the hidden encoder vector assessed from x_n, and $\hat{x}$ denotes the decoding vector of output. Thus, using the following equation, the encoder process can be performed:

$$h_n = f(W_1 x_n + b_1) \tag{5}$$

Now, f denotes the encoder function, W_1 indicates the weighted matrix of encoding function, and b_1 shows the bias vector. Using the given formula, the decoder method can be determined:

$$\hat{x}_n = g(W_2 h_n + b_2) \tag{6}$$

Where g shows the decoder function, W_2 indicates the weight matrices of the decoding function, and b_2 represent the bias vector.

The parameter set of the AE is improvised to reduce the reconstructed error:

$$(\phi(\Theta) = \arg_{\theta,\theta'} min \frac{1}{n} \sum_{i=1}^{n} L\left(x^i, \hat{x}^i\right) \tag{7}$$

Here, L indicates the loss function $L(x, \hat{x}) = \|x - \hat{x}\|^2$. The architecture of SAE is stacking n autoencoder into n hidden layer through the unsupervised layer-wise learning mechanism and fine-tuned through a supervised manner. Fig. 3 depicts the infrastructure of SAE. As a result, the SAE based method can be categorized by the following:

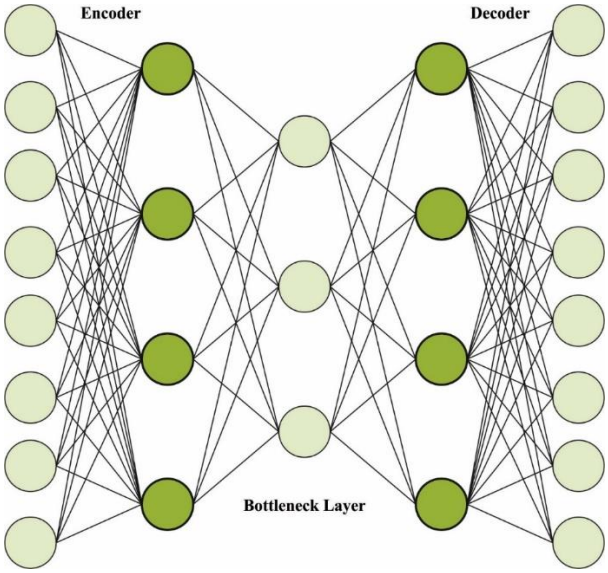

Figure. 3 Architecture of SAE

1) The initial AE is trained through input dataset and accomplishes the learned feature vector;
2) The feature vector of preceding layers is employed as the input for the subsequent layers, and the procedure is reiterated until the training ends.

Then, backpropagation (BP) minimizes the cost function and updates the weight through labelled training subsets to accomplish fine-tuning.

3.5 HHO based hyperparameter optimization process

Finally, the HHO technique is applied to optimally tune the hyperparameter related to the SAE model. HHO is a metaheuristic technique and is executed as different solution for difficult challenges [24]. HHO is dependent upon the performance of Harris hawks are intelligent birds. It takes a mechanism which allows them for tracing the target while it could escape. This procedure was demonstrated by mathematical equation that permits computation implementation. HHO suggests to stochastic system which is define complicated search spaces for exploring optimum feasible solutions. The basic stages of HHO can be attained with concern for various states of energy. At the time of exploration, the hawks get a halt for locating and tracking new candidate solutions hawked in the HHO technique, and a better solution in all the steps is prey. The hawk perches at various positions and waits for the prey employing 2 functions that are selected depending upon the probability q as demonstrated under If $q < 0.5$ identifies that the hawk arbitrarily perching at the location of another member of populations and prey (i.e., rabbit) and it can be expressed from the formula

$$X(n+1) = \begin{Bmatrix} X_{rand}(n) - r_1|X_{rand}(n) - 2r_2X(n)| \\ q \geq 0.5 \\ \big(X_{rab}(n) - X_m(n)\big) - r_3\big(LB + r_4(UB - LB)\big) \\ q < 0.5 \end{Bmatrix} \quad (8)$$

The average location of Hawks X_m was provided in the following:

$$X_m(n) = \frac{1}{N}\sum_{i=1}^{N} X_i\,(n) \quad (9)$$

Assume $X(n)$ be the iteration place for all the Hawks n and N signifies the entire Hawk count. The average place was obtained by different methods, but, it can be an easy principle. An optimal shift in exploration to exploitation is important, due to the escape energy factor EF which significantly decreases the escape method and it could be defined as:

$$E = 2E_0\left(1 - \frac{n}{N}\right) \quad (10)$$

In Eq. (10), E_0 and T denotes the initial escaping energy and the higher count of iterations. The soft besiege is considerable step from HHO, in which $r \geq 0.5$ and $|EF| \geq 0.5$. During these situations, the rabbit has suitable energy. The besiege stage was determined by:

$$X(n+1) = \triangle X(n) - EF|JX_{rab}(n) - X(n)| \quad (11)$$

$$\triangle X(n) = X_{rab}(n) - X(n) \quad (12)$$

In the formula, $\triangle X(n)$ implies the position vector to all the rabbits and for current place in the iteration t, and $J = 2(1 - r\_5)$ represents the rabbit's spontaneous jump ability all around the escape step. The J value arbitrarily varies from all the iterations to characterize the rabbit efficiency. If $r \geq 0.5$ and $|EF| < 0.5$, the prey has been exhausted and is no escape power. In these cases, the current place has been changed by the following equation:

$$X(n+1) = X_{rab}(n) - EF|\triangle X(n)| \quad (13)$$

Assuming the hawk's performance in real-time, it can progressively select the finest dive to prey when it needs to catch the objective in good state:

$$Y = X_{rab}(n) - EF|JX_{rab}(n) - X(n)| \quad (14)$$

Algorithm 2: Pseudocode of HHO Algorithm

Produce arbitrary hawks population $X_i(i = 1,2 \dots, n)$
Evaluate the fitness values of each Hawk
$X_{rab\text{bit}}$ is the rabbit location (better solution)
$w$hile (t <maximal iteration counts)
    for every hawk (X_i)
        Upgrading the first energy E_0
        Upgrading the prey energy EF
        Upgrading the jump strength J
        if ($|EF] \geq 1$)
            Upgrading the location of current solutions
        endif
        if ($|EF| < 1$)
            $if\ (r \geq 0.5 and |E\ | \geq 0.5)$
                Upgrading the location of present solution
            $elseif (r \geq 0.5\ and\ |E| < 0.5\ )$
                Upgrading the location of current solution
            $elseif\ (r < 0.5\ and\ \ |E| \geq 0.5)$
                Upgrading the place of existing solution
            $elseif\ (r < 0.5\ and\ |E| < 0.5)$
                Upgrading the location of present solution
        endif
    endfor
Validate when any solution develops above the search space and modify it
Calculate the fitness of every Hawk
When better solution exists, upgrading X_{rab}
n=n+1
endwhile
Return X_{rab}

The soft besiege predefining in the earlier Eq. (14) was executed from progressive rapid dive if $|E| \geq 0.5$ then $r < 0.5$. In that case, the rabbit has sufficient energy to escape and is utilized to soft siege previously the assault comes as surprise. The HHO technique is varied escape patterns for prey movement and leap frogs. At this time, the Lévy flights (LF) can be established to follow the Hawk movement and rabbit dives as follows.

$$Z = Y + S \times LF(D) \tag{15}$$

In Eq. (15), S stands for the arbitrary vector for size 1xD and LF implies the LF function:

$$LF(x) = 0.01 \times \frac{u \times \sigma}{|v|^{\frac{1}{\beta}}}, \sigma = \left(\frac{\Gamma(1+\beta) \times \sin\left(\frac{\pi\beta}{2}\right)}{\Gamma\left(\frac{1+\beta}{2}\right) \times \beta \times 2^{\left(\frac{\beta-1}{2}\right)}} \right)^{\frac{1}{\beta}} \tag{16}$$

At this point, u, v signifies the arbitrary values betwixt zero and one, β implies the constant set as 1.5. The final stage is to upgrade the hawk's position:

$$X(n+1) = \begin{cases} y & if\ F(Y) < F\big(X(n)\big) \\ Z & if\ F(Z) < F\big(X(n)\big) \end{cases} \tag{17}$$

Now, y and Z are obtained utilizing Eqs. (13) and (14). The rabbit's energy to escape could not be suitable and hard siege has suggested previously the surprise attack was aimed to catch and kill the goal. At this point, the Hawks reduce the distance betwixt the average place and its prey:

$$X(n+1) = \begin{cases} Y & if\ F(Y) < F\big(X(n)\big) \\ Z & if\ F(Z) < F\big(X(n)\big) \end{cases} \tag{18}$$

y and Z values utilize new procedures in Eqs. (19) and (20), thus X_m (t) was obtained using Eq. (19).

$$Y = X_{rabbit}(n) - E|Jx_{rab(n)} - X_m(n)| \tag{19}$$

$$Z = Y + S \times LF(D) \tag{20}$$

Fitness selection is a key factor in the HHO technique. Solution encoding is applied to assess the aptitude (goodness) of candidate solution. At present, the

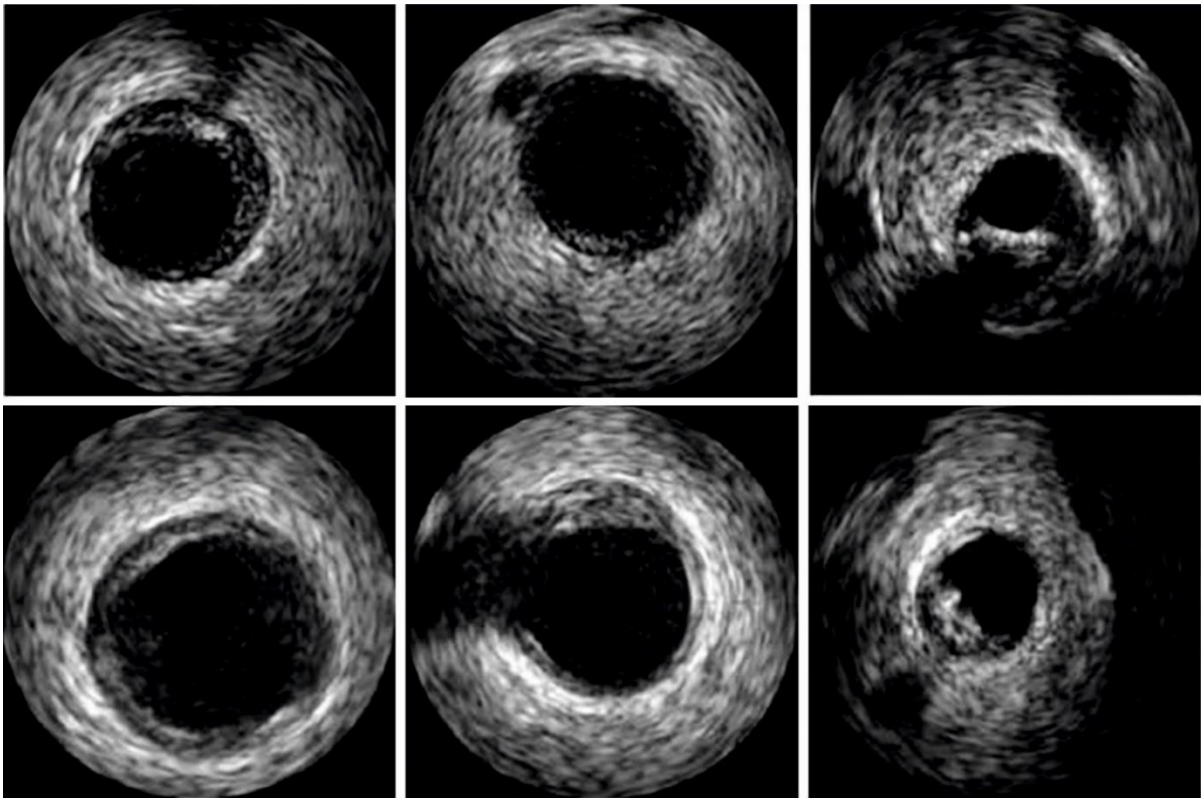

Figure. 4 Sample images

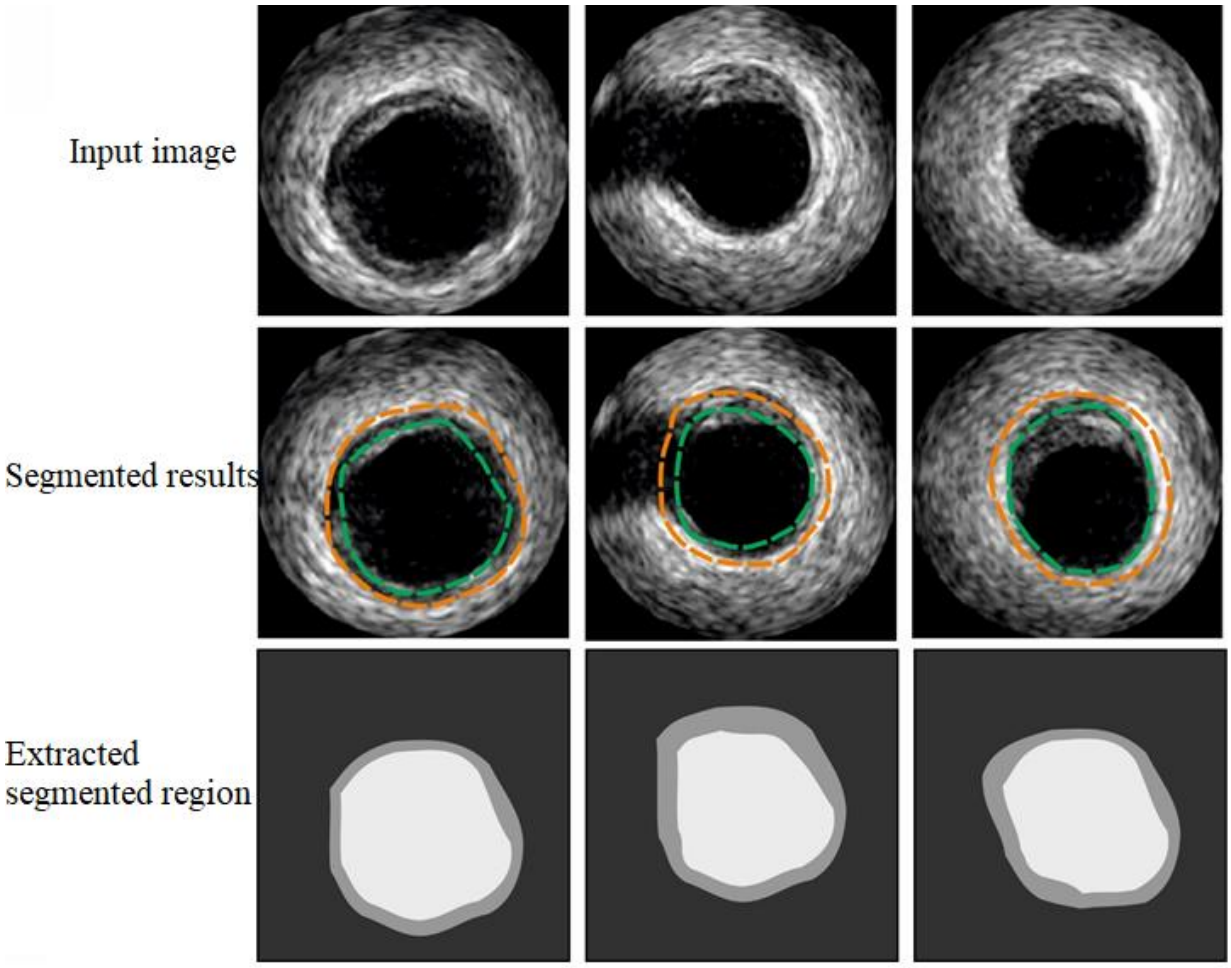

Figure. 5 Sample segmentation results

Table 2. Overall segmentation outcome of ODTL-APCIUI approach

Measures	DSC	Precision	Sensitivity	Specificity	Avg. Precision
Focal Loss					
Media-Adventitia	98.17±0.8	89.53±2.3	97.71±1.6	95.19±0.9	88.97±0.5
Lumen	97.05±1.4	88.97±0.2	97.58±0.5	94.81±2.7	86.06±0.9
Calcification	97.88±1.1	90.91±0.9	98.04±0.5	96.06±2.7	87.75±0.9
Dice Loss					
Media-Adventitia	93.72±1.5	97.57±1.5	93.06±1.1	98.67±1	92.48±2
Lumen	91.98±1.1	97.14±2.8	92.52±1.6	98.5±2.2	92.04±2.4
Calcification	94.16±1.6	98.48±2.1	94.2±2.3	99.08±1.1	93.49±1.6
Tversky Loss					
Media-Adventitia	96.82±1.1	97.25±0.2	97±0.8	96.55±2.7	96.74±0.1
Lumen	96.23±2.3	95.75±2.8	96.48±0.1	95.9±0.6	94.45±0.8
Calcification	97.97±2.4	98.22±2.5	98.28±0.9	98.31±1.8	95.31±0.3

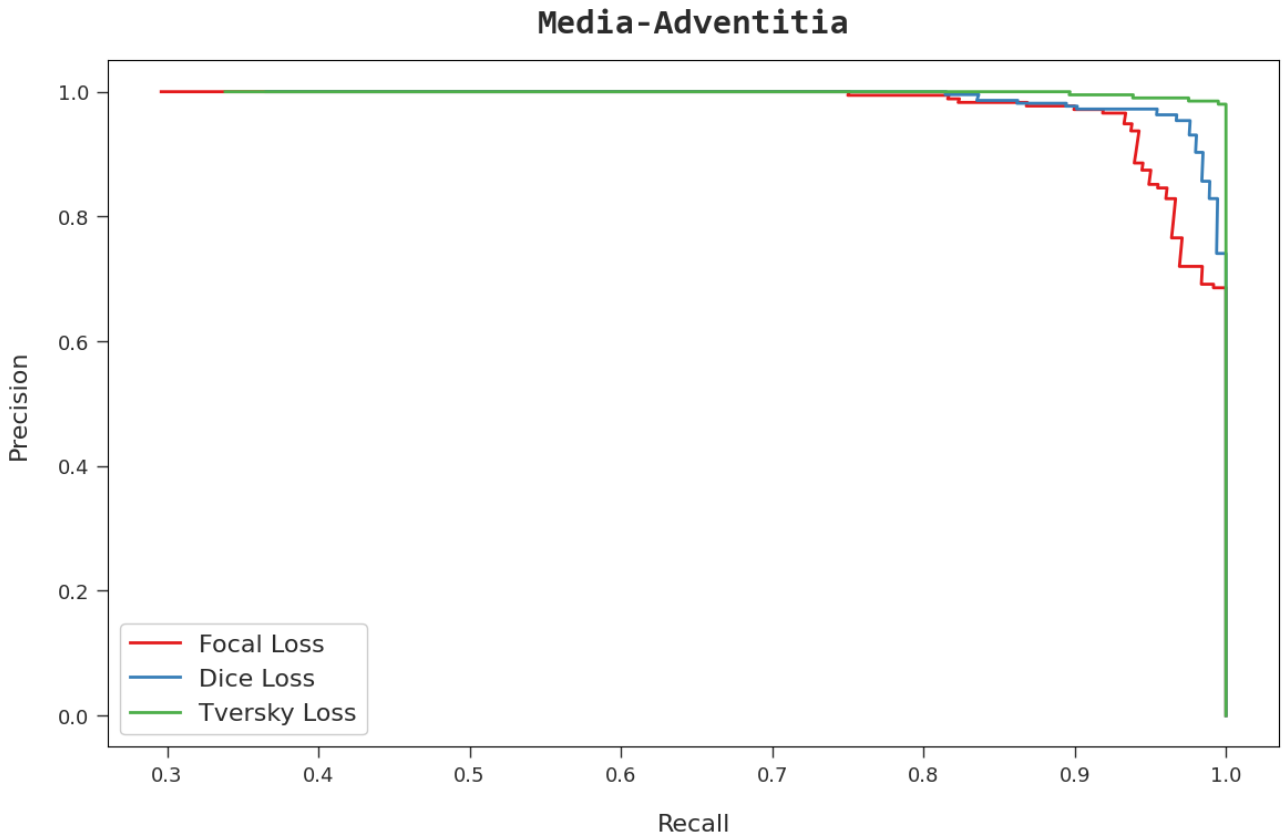

Figure. 6 Precision-recall analysis of ODTL-APCIUI method under media-adventitia

accuracy value is the main condition exploited to design the fitness function.

$$Fitness = \max(P) \quad (21)$$

$$P = \frac{TP}{TP+FP} \quad (22)$$

From the expression, TP represents the true positive and FP denotes the false positive value

4. Results and discussion

In this section, the experimental validation of ODTL-APCIUI technique takes place using dataset B from MICCAI challenge-2011 [25]. The dataset holds 2175 images from 10 persons, 1645 with

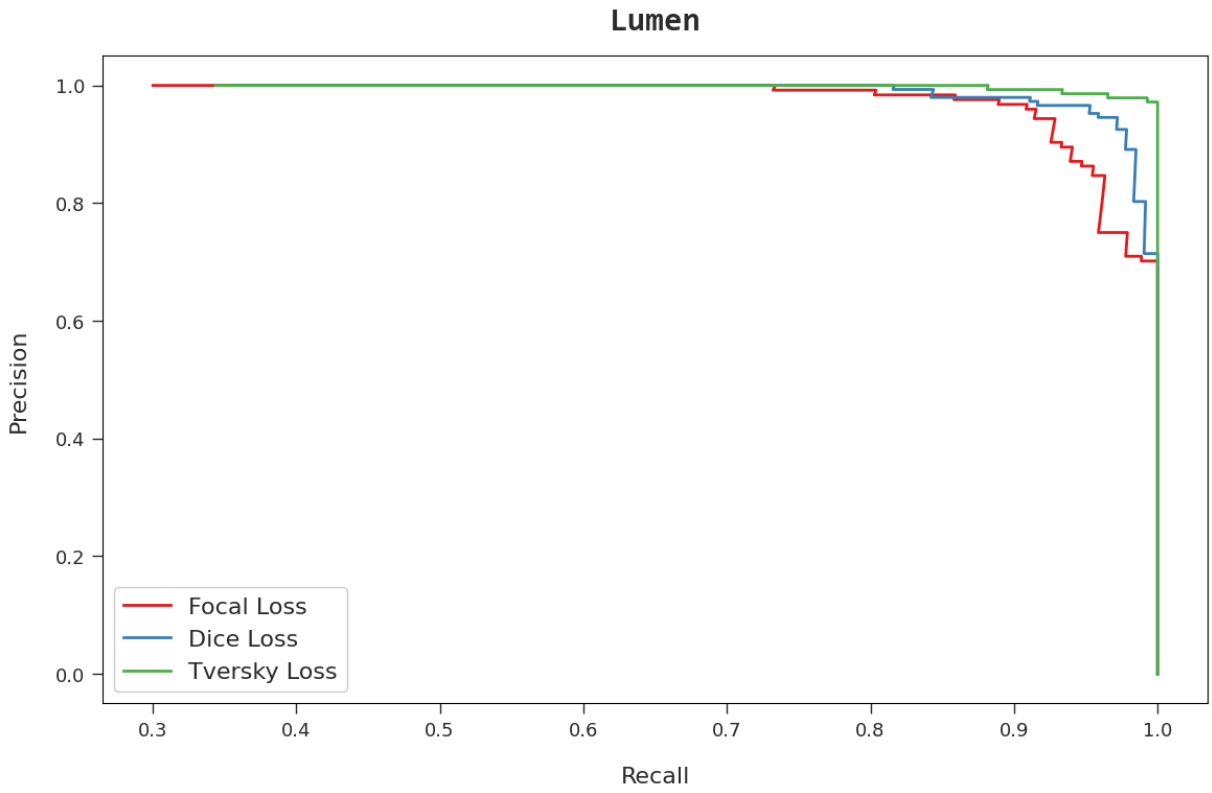

Figure. 7 Precision-recall analysis of ODTL-APCIUI technique under lumen

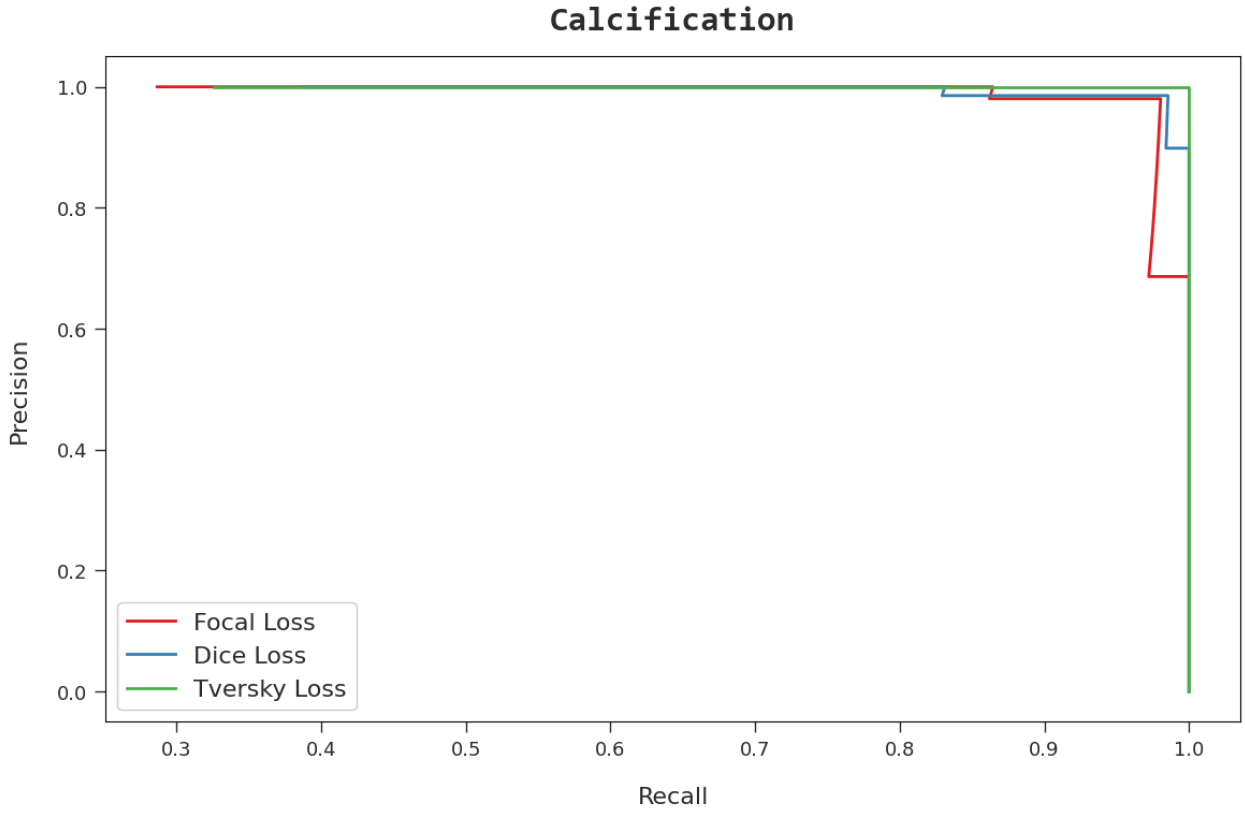

Figure. 8 Precision-recall analysis of ODTL-APCIUI technique under calcification

calcification absent or plaque composites and 530 images with present calcification. Fig. 4 depicts the sample images.

Fig. 5 shows the sample segmentation results of the proposed model on the IVUS image. The figure indicated that the proposed model has properly

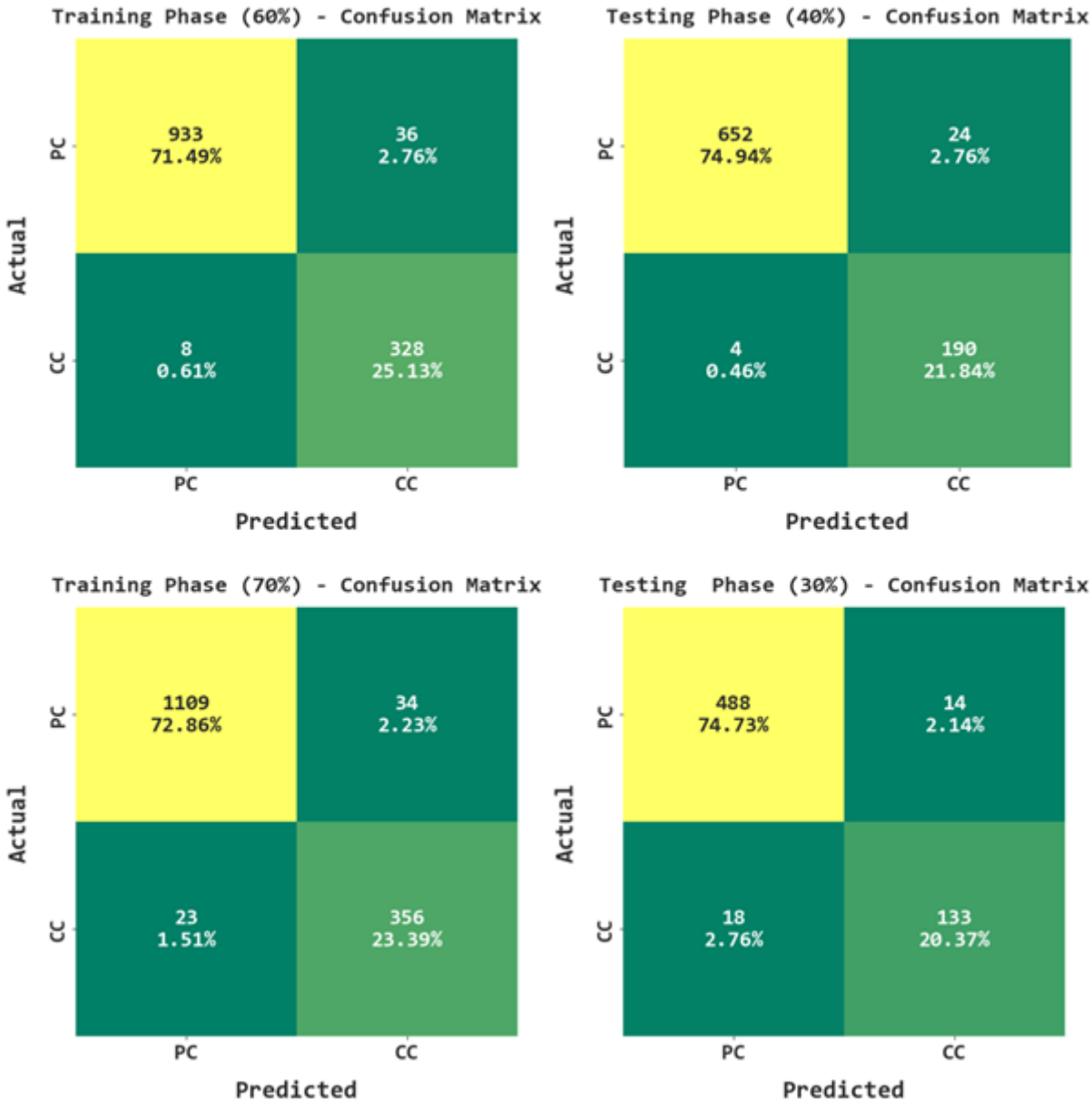

Figure. 9 Confusion matrices of ODTL-APCIUI methodology TRS and TSS of 60:40 and TRS and TSS of 70:30

Table 3. Details of dataset

Class	No. of Samples
Plaque Composites (PC)	1645
Calcification Composites (CC)	530
Total No. of Samples	2175

segmented the regions closer to the ground truth regions.

Table 2 represents the overall segmentation results of the ODTL-APCIUI technique. The result indicates that the ODTL-APCIUI technique has reached effectual outcomes under focal loss, dice loss, and Tversky loss.

Fig. 6 shows the precision-recall study of the ODTL-APCIUI technique under media-adventitia. The results indicated that the ODTL-APCIUI technique has reached increasing values of precision-recall under all aspects. Fig. 7 shows the precision-recall investigation of the ODTL-APCIUI approach under lumen. The outcomes show that the ODTL-APCIUI method has attained maximum values of precision-recall under all aspects. Next, Fig. 8 illustrates the precision-recall examination of the ODTL-APCIUI system under calcification. The outcome indicates that the ODTL-APCIUI technique has attained increasing values of precision-recall under all aspects.

The classification performance of the ODTL-APCIUI system can be examined using the dataset comprising 1645 PC and 530 CC samples as depicted in Table 3.

Table 4. Overall outcome of ODTL-APCIUI approach on 60:40 of TRS/TSS

Class	$Accuracy_{bal}$	Precision	Sensitivity	Specificity	F-Score	NPV
Training Phase (60%)						
PC	96.28	99.15	96.28	97.62	97.70	90.11
CC	97.62	90.11	97.62	96.28	93.71	99.15
Average	**96.95**	**94.63**	**96.95**	**96.95**	**95.71**	**94.63**
Testing Phase (40%)						
PC	96.45	99.39	96.45	97.94	97.90	88.79
CC	97.94	88.79	97.94	96.45	93.14	99.39
Average	**97.19**	**94.09**	**97.19**	**97.19**	**95.52**	**94.09**

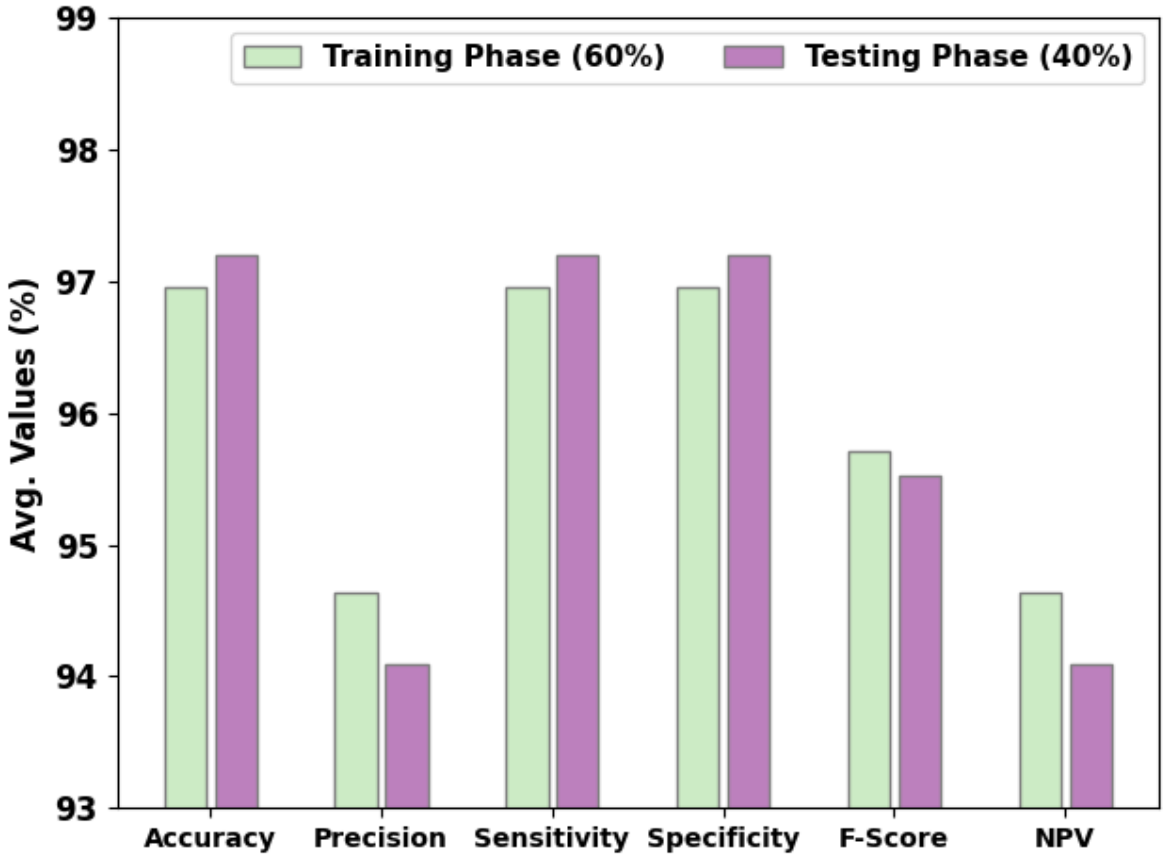

Figure. 10 Average outcome of ODTL-APCIUI approach on 60:40 of TRS/TSS

The confusion matrices of the ODTL-APCIUI technique are demonstrated in Fig. 9. The results pointed out that the ODTL-APCIUI method has detected PC and CC samples accurately. For instance, with 60% of TRS data, the ODTL-APCIUI technique has detected 933 samples under PC class and 328 samples under CC class. Meanwhile, with 40% of TS data, the ODTL-APCIUI system has detected 652 samples under PC class and 190 samples under CC class. Eventually, with 40% of TSS data, the ODTL-APCIUI system has detected 1109 samples under PC class and 356 samples under CC class.

Table 4 and Fig. 10 report the overall results of the ODTL-APCIUI technique on 60:40 of TRS/TSS. The results indicated that the ODTL-APCIUI technique has effectually identified PC and CC classes. For instance, on 60% of TRS, the ODTL-

Table 5. Overall outcome of ODTL-APCIUI approach on 70:30 of TRS/TSS

Class	$Accuracy_{bal}$	Precision	Sensitivity	Specificity	F-Score	NPV
Training Phase (70%)						
PC	97.03	97.97	97.03	93.93	97.49	91.28
CC	93.93	91.28	93.93	97.03	92.59	97.97
Average	**95.48**	**94.63**	**95.48**	**95.48**	**95.04**	**94.63**
Testing Phase (30%)						
PC	97.21	96.44	97.21	88.08	96.83	90.48
CC	88.08	90.48	88.08	97.21	89.26	96.44
Average	**92.65**	**93.46**	**92.65**	**92.65**	**93.04**	**93.46**

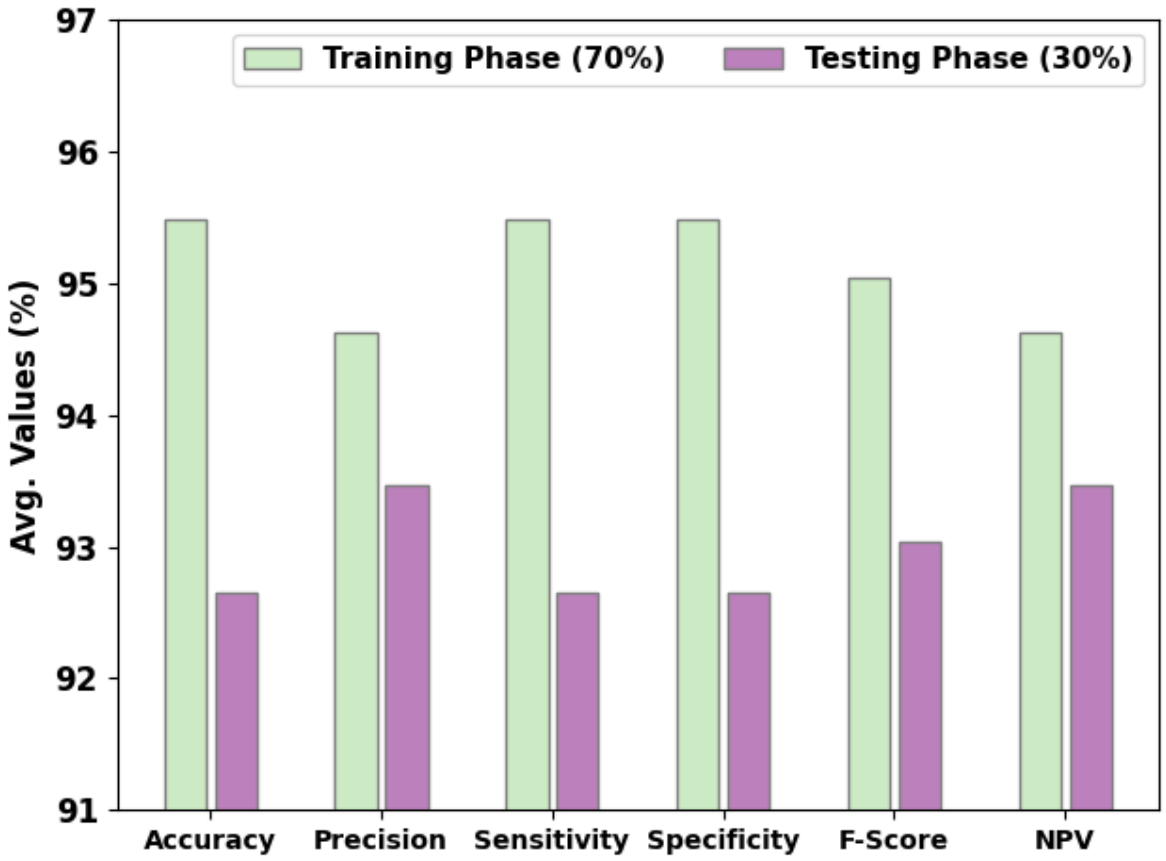

Figure. 11 Average outcome of ODTL-APCIUI approach on 70:30 of TRS/TSS

APCIUI technique has obtained average $accu_{bal}$ of 96.95%, $prec_n$ of 94.63%, $sens_y$ of 96.95%, $spec_y$ of 96.95%, F_{score} of 95.71%, and NPV of 94.63%. At the same time, on 40% of TSS, the ODTL-APCIUI method has attained average $accu_{bal}$ of 97.19%, $prec_n$ of 94.09%, $sens_y$ of 97.19%, $spec_y$ of 97.19%, F_{score} of 95.52%, and NPV of 94.09%.

Table 5 and Fig. 11 show the overall outcomes of the ODTL-APCIUI system on 60:40 of TRS/TSS. The result indicates that the ODTL-APCIUI technique effectively recognizes PC and CC classes. For example, on 70% of TRS, the ODTL-APCIUI technique has obtained average $accu_{bal}$ of 96.95%, $prec_n$ of 94.63%, $sens_y$ of 96.95%, $spec_y$ of 96.95%, F_{score} of 95.71%, and NPV of 94.63%. Simultaneously, on 30% of TSS, the ODTL-APCIUI method has gained average $accu_{bal}$ of 92.65%, $prec_n$ of 93.46%, $sens_y$ of 92.65%, $spec_y$ of 92.65%, F_{score} of 93.04%, and NPV of 93.46%.

The TACC and VACC of the ODTL-APCIUI approach are investigated on IVUS performance in

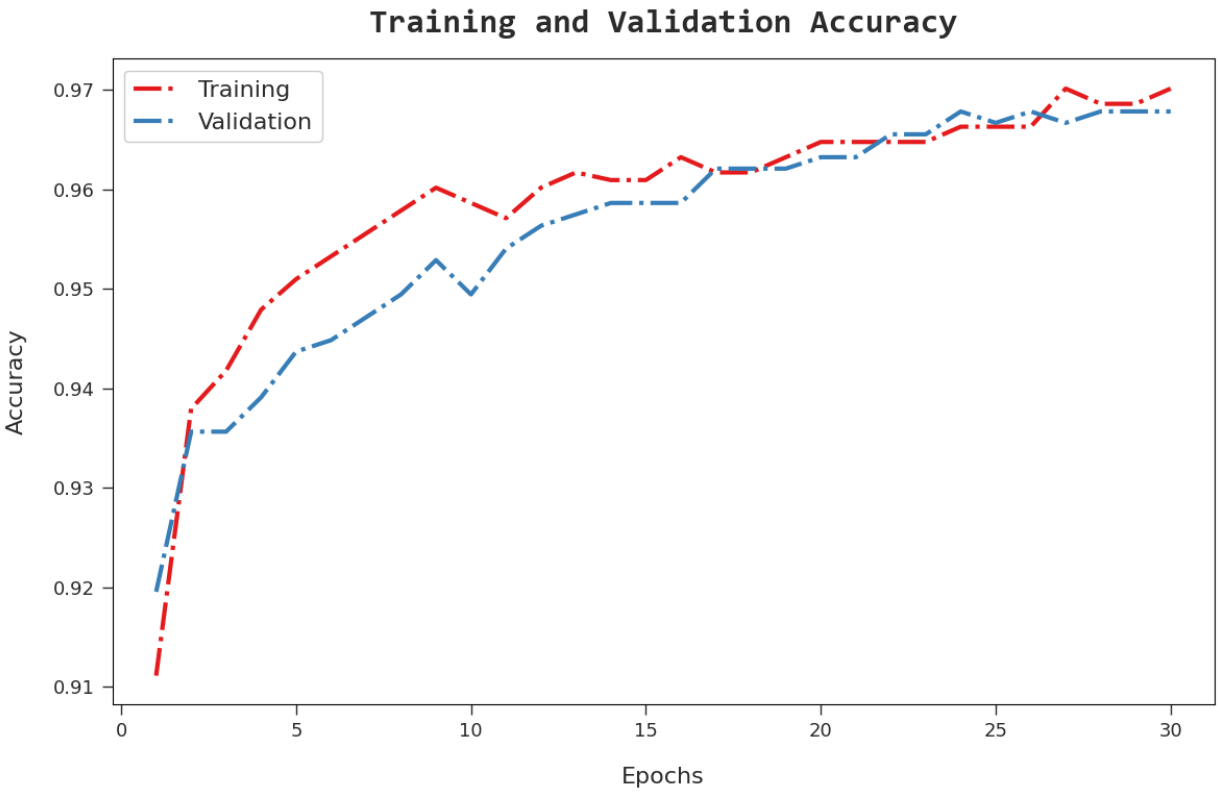

Figure. 12 TACC and VACC analysis of ODTL-APCIUI approach

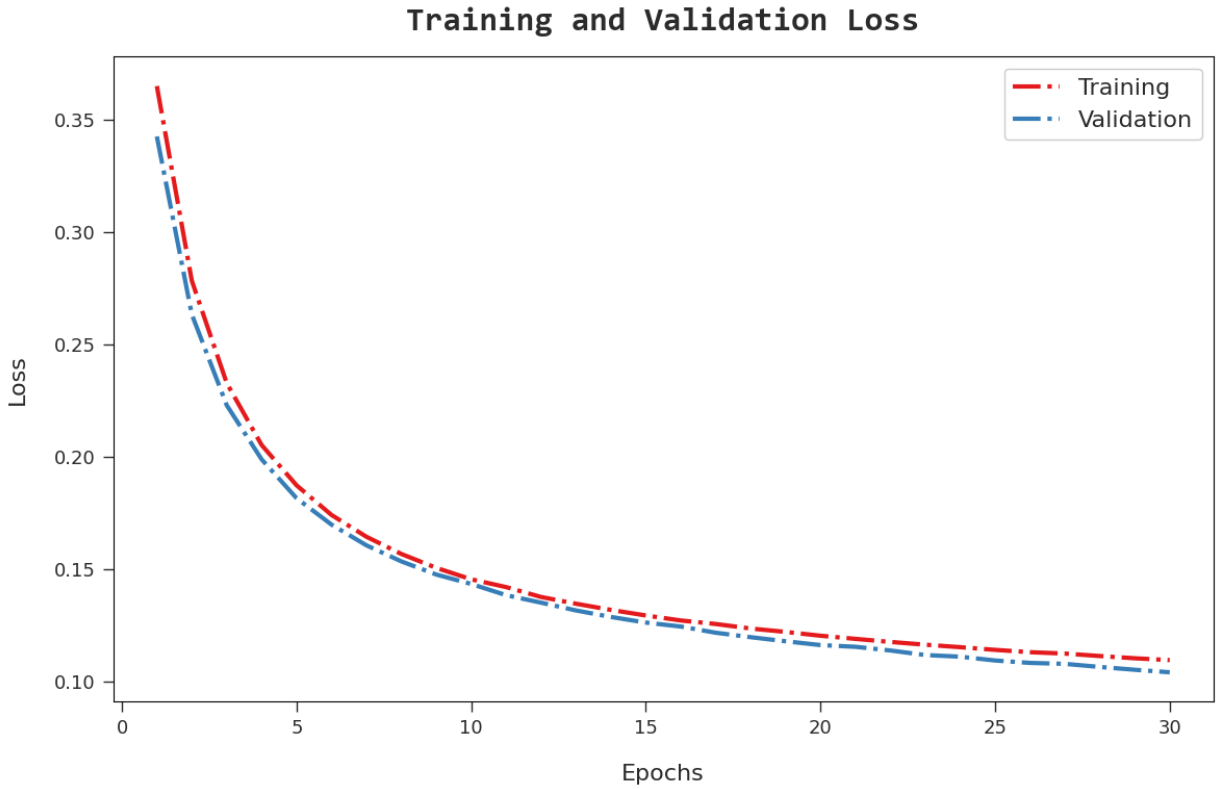

Figure. 13 TLS and VLS analysis of ODTL-APCIUI approach

Fig. 12. The figure shows that the ODTL-APCIUI system has shown improved performance with increased values of TACC and VACC. It is noted that the ODTL-APCIUI model has attained maximum TACC outcomes. The TLS and VLS of the ODTL-APCIUI technique are tested on IVUS performance in Fig. 13. The figure inferred that the ODTL-APCIUI method has revealed better performance

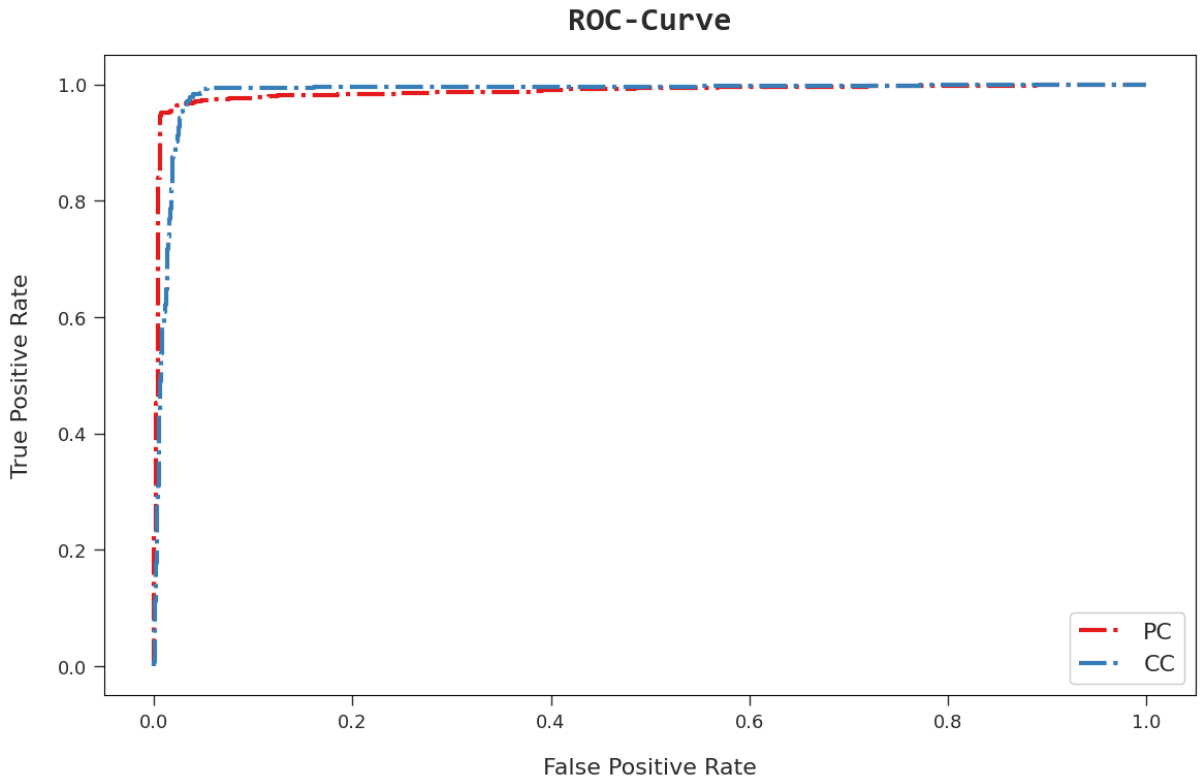

Figure. 14 ROC analysis of ODTL-APCIUI approach

Table 6. Comparative analysis of ODTL-APCIUI with existing techniques

Methods	$Accuracy_{bal}$	Precision	Sensitivity	Specificity	F-Score
ODTL-APCIUI	97.19	94.09	97.19	97.19	95.52
DL Model [13]	94.02	93.43	94.70	91.49	93.29
ADF-AS [26]	91.94	90.51	94.08	91.94	93.02
ASCP-VB [27]	91.93	93.79	94.57	94.22	93.66
KNN Classifier [17]	92.57	90.71	92.70	93.08	93.94
DT Classifier [17]	92.10	93.43	92.78	93.31	91.00
NB Classifier [17]	91.27	93.52	92.45	94.50	93.20

with least values of TLS and VLS. It is noted that the ODTL-APCIUI approach has resulted in minimum VLS outcomes.

A brief ROC examination of the ODTL-APCIUI approach under test database is depicted in Fig. 14. The outcome shows the ODTL-APCIUI method has shown its capability in classifying different classes under test database.

To validate the performance of the ODTL-APCIUI model with recent models, a comparison study is given in Table 6 [13, 17, 26, 27]. Fig. 15 represents the comparative study of the ODTL-APCIUI with existing models in terms of $accu_{bal}$, $prec_n$, and F_{score}. The results show that the ADF-AS, ASCP-VB, and NB models have reported lower performance with closer $accu_{bal}$, $prec_n$, and F_{score}. In addition, the KNN and DT classification models have revealed the certainly somewhat improved values of $accu_{bal}$, $prec_n$, and F_{score}. Next, the DL model has accomplished reasonable outcomes with $accu_{bal}$, $prec_n$, and F_{score} of 94.02%, 93.43%, and 93.29% respectively. But the ODTL-APCIUI technique has accomplished maximum $accu_{bal}$, $prec_n$, and F_{score} of 97.19%, 94.09%, and 95.52%.

Fig. 16 characterizes the comparison analysis of the ODTL-APCIUI with current techniques in terms of, $sens_y$, and $spec_y$. The result demonstrates that the ADF-AS, ASCP-VB, and NB approaches have reported lower performance with closer $sens_y$, and $spec_y$. Furthermore, the KNN and DT classification

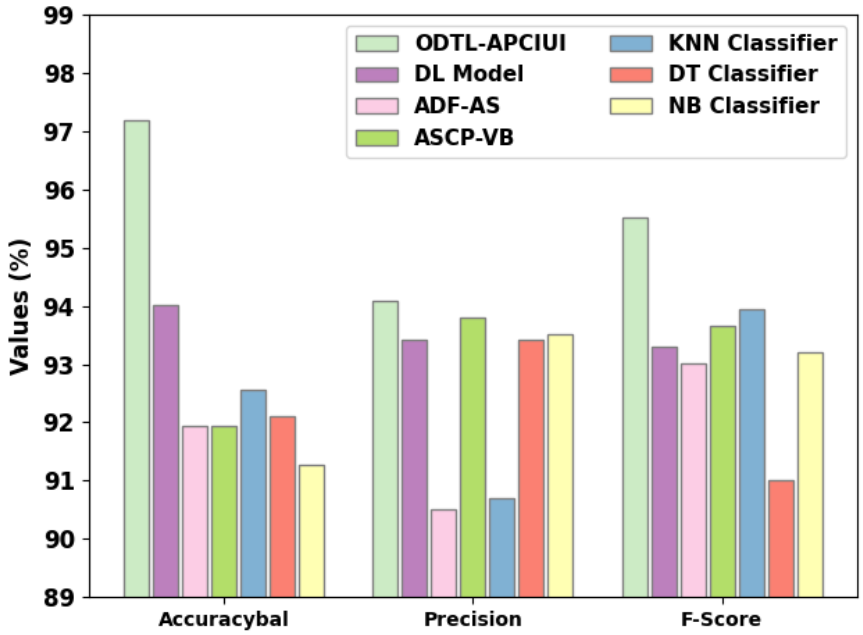

Figure. 15 Comparative analysis of ODTL-APCIUI approach with existing methodologies

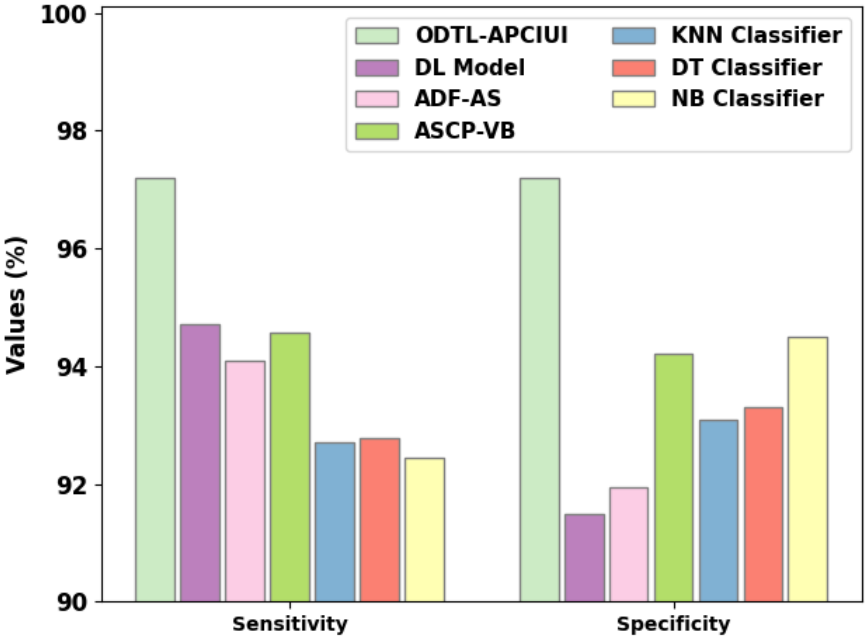

Figure. 16 $Sens_y$ and $Spec_y$ analysis of ODTL-APCIUI approach with existing methodologies

techniques have revealed the certainly somewhat improved values of $sens_y$, and $spec_y$ Next, the DL approach has accomplished reasonable outcomes with, $sens_y$, and $spec_y$ of 94.70% and 91.49% correspondingly.

But the ODTL-APCIUI technique has accomplished maximal $sens_y$, and $spec_y$ of 97.19% and 97.19%. These results highlighted that the ODTL-APCIUI technique has accomplished maximum performance on Atherosclerotic Plaque and Calcification.

5. Conclusion

In this study, we have developed a new ODTL-APCIUI approach for the classification of calcification and atherosclerotic plaque on the IVUS images. The presented ODTL-APCIUI technique encompasses HHO based hyperparameter tuning, GF based preprocessing, U-Net segmentation,

DenseNet-169 feature extraction, and SAE based classification. The performance assessment of the ODTL-APCIUI approach is tested under medical images and the results are investigated under different metrics. The experimental outcomes showed that the ODTL-APCIUI technique has attained better performance than other techniques with maximum accuracy of 97.19%, precision of 94.09%, sensitivity of 97.17%, specificity of 97.19%, and F-score of 92.52%. Thus, the presented ODTL-APCIUI technique can be applied for automated classification of IVUS images. In the future, the performance of ODTL-APCIUI algorithm can be improved by the use of ensemble learning process.

Conflicts of interest

The authors declare no conflict of interest

Author contributions

For this research work all authors have equally contributed in Conceptualization, Methodology, validation, resources, writing- original draft preparation, writing-review and editing.

References

[1] S H. Shinohara, S. Kodera, K. Ninomiya, M. Nakamoto, S. Katsushika, A. Saito, S. Minatsuki, H. Kikuchi, A. Kiyosue, Y. Higashikuni, N. Takeda, K. Fujiu, J. Ando, H. Akazawa, H. Morita, and I. Komuro, "Automatic detection of vessel structure by deep learning using intravascular ultrasound images of the coronary arteries", *Plos One*, Vol. 16, No. 8, 2021.

[2] M. Terashima, H. Kaneda, Y. Honda, T. Shimura, A. Kodama, M. Habara, and T. Suzuki, "Current status of hybrid intravascular ultrasound and optical coherence tomography catheter for coronary imaging and percutaneous coronary intervention", *Journal of Cardiology*, Vol. 77, No. 5, pp. 435–443, 2021.

[3] C. Peng, H. Wu, S. Kim, X. Dai, and X. Jiang, "Recent advances in transducers for intravascular ultrasound (IVUS) imaging", *Sensors*, Vol. 21, No. 10, p. 3540, 2021.

[4] R. Bajaj, J. Eggermont, S. J. Grainger, L. Räber, R. Parasa, A. H. Khan, C. Costa, E. Erdogan, M. J. Hendricks, K. H. Chandrasekharan, M. Andiapen, P. W. Serruys, R. Torii, A. Mathur, A. Baumbach, J. Dijkstra, and C. V. Bourantas, "Machine learning for atherosclerotic tissue component classification in combined near-infrared spectroscopy intravascular ultrasound imaging: Validation Against Histology", *Atherosclerosis*, Vol. 345, pp. 15–25, 2022.

[5] E. Akl, N. P. Echeverri, H. M. G. Garcia, S. R. Mehta, K. Dan, K. O. Kuku, B. K. Courtney, and T. Sheth, "First in-human evaluation of a novel intravascular ultrasound and optical coherence tomography system for intracoronary imaging", *Catheterization and Cardiovascular Interventions*, Vol. 99, No. 3, pp. 686–698, 2021.

[6] K. V. Archana and R. V. R. Vanithamani, "Segmentation of intima – media thickness in intravascular ultrasound images for detection of atherosclerosis", *Biomedical and Pharmacology Journal*, Vol. 15, No. 3, pp. 1539–1549, 2022.

[7] X. Gao, Y. Wang, and J. Sun, "Intravascular ultrasound image plaque recognition based on improved Resnet Network", In: *Proc. of 2022 7th International Conference on Intelligent Computing and Signal Processing (ICSP)*, 2022.

[8] Y. Wang, X. Gao, Y. Wang, and J. Sun, "Adventitia segmentation in intravascular ultrasound images based on improved snake algorithm", *Optik*, Vol. 241, p. 167175, 2021.

[9] C. Homorodean, D. C. Leucuta, M. Ober, R. Homorodean, M. Spinu, M. Olinic, D. Tataru, and D. M. Olinic, "Intravascular ultrasound insights into the unstable features of the coronary atherosclerotic plaques: A systematic review and meta-analysis", *European Journal of Clinical Investigation*, Vol. 52, No. 1, 2021.

[10] A. Gudigar, S. Nayak, J. Samanth, U. Raghavendra, A. A. J. P. D. Barua, M. N. Hasan, E. J. Ciaccio, R. S. Tan, and U. R. Acharya, "Recent trends in artificial intelligence-assisted coronary atherosclerotic plaque characterization", *International Journal of Environmental Research and Public Health*, Vol. 18, No. 19, p. 10003, 2021.

[11] L. Bargsten, S. Raschka, and A. Schlaefer, "Capsule Networks for segmentation of small intravascular ultrasound image datasets", *International Journal of Computer Assisted Radiology and Surgery*, Vol. 16, No. 8, pp. 1243–1254, 2021.

[12] R. Bajaj, X. Huang, Y. Kilic, A. Ramasamy, A. Jain, M. Ozkor, V. Tufaro, H. Safi, E. Erdogan, P. W. Serruys, J. Moon, F. Pugliese, A. Mathur, R. Torii, A. Baumbach, J. Dijkstra, Q. Zhang, and C. V. Bourantas, "Advanced deep learning methodology for accurate, real-time segmentation of high-resolution intravascular ultrasound images", *International Journal of Cardiology*, Vol. 339, pp. 185–191, 2021.

[13] Y. C. Li, T. Y. Shen, C. C. Chen, W. T. Chang, P. Y. Lee, and C. C. J. Huang, "Automatic

detection of atherosclerotic plaque and calcification from intravascular ultrasound images by using deep convolutional neural networks", *IEEE Transactions on Ultrasonics, Ferroelectrics, and Frequency Control*, Vol. 68, No. 5, pp. 1762–1772, 2021.

[14] H. Sofian, J. C. M. Than, S. Mohamad, and N. M. Noor, "Calcification detection for intravascular ultrasound image using direct acyclic graph architecture: Pre-trained model for 1-channel image", *Indonesian Journal of Electrical Engineering and Computer Science*, Vol. 22, No. 2, p. 787, 2021.

[15] S. Liu, T. Neleman, E. M. J. Hartman, J. M. R. Ligthart, K. T. Witberg, A. F. W. V. D. Steen, J. J. Wentzel, J. Daemen, and G. V. Soest, "Automated Quantitative Assessment of coronary calcification using intravascular ultrasound", *Ultrasound in Medicine & Biology*, Vol. 46, No. 10, pp. 2801–2809, 2020.

[16] H. Cho, S. J. Kang, H. S. Min, J. G. Lee, W. J. Kim, S. H. Kang, D. Y. Kang, P. H. Lee, J. M. Ahn, D. W. Park, and S. W. Lee, "Intravascular Ultrasound-Based Deep Learning for Plaque Characterization in Coronary Artery Disease", *Atherosclerosis*, Vol. 324, pp. 69–75. 2021.

[17] H. Sofian, J. C. Than, S. Mohammad, and N. M. Noor, "Using deep learning for calculation detection in coronary artery disease intravascular ultrasound image", In: *Proc. of Applied Physics of Condensed Matter (APCOM 2019)*, 2019.

[18] L. Dong, W. Jiang, W. Lu, J. Jiang, Y. Zhao, X. Song, X. Leng, H. Zhao, J. Wang, C. Li, and J. Xiang, "Automatic segmentation of coronary lumen and external elastic membrane in intravascular ultrasound images using 8-layer U-Net", *BioMedical Engineering OnLine*, Vol. 20, No. 1, 2021.

[19] J. Zeng, X. Qiu, and S. Shi, "Image processing effects on the deep face recognition system", *Mathematical Biosciences and Engineering*, Vol. 18, No. 2, pp. 1187-1200, 2021.

[20] X. Qin, Z. Zhang, C. Huang, M. Dehghan, O. R. Zaiane, and M. Jagersand, "U2-net: Going deeper with nested U-structure for salient object detection", *Pattern Recognition*, Vol. 106, p. 107404, 2020.

[21] A. H. Khan, X. Cao, S. Li, V. N. Katsikis, and L. Liao, "Bas-Adam: An adam based approach to improve the performance of beetle Antennae Search optimizer", *IEEE/CAA Journal of AutomaticaSinica*, Vol. 7, No. 2, pp. 461–471, 2020.

[22] F. BabapourMofrad and G. Valizadeh, "DenseNet-based transfer learning for LV shape classification: Introducing A novel information fusion and data augmentation using statistical shape/colormodeling", *Expert Systems with Applications*, Vol. 213, p. 119261, 2023.

[23] M. Yu, T. Quan, Q. Peng, X. Yu, and L. Liu, "A model-based collaborate filtering algorithm based on stacked AutoEncoder", *Neural Computing and Applications*, Vol. 34, No. 4, pp. 2503–2511, 2021.

[24] R. J. Kavitha, C. Thiagarajan, P. I. Priya, A. V. Anand, E. A. A. Ammar, M. Santhamoorthy, and P. Chandramohan, "Improved harrishawks optimization with hybrid deep learning based heating and cooling load prediction on residential buildings", *Chemosphere*, Vol. 309, p. 136525, 2022.

[25] S. Balocco, C. Gatta, F. Ciompi, A. Wahle, P. Radeva, S. Carlier, G. Unal, E. Sanidas, J. Mauri, X. Carillo, T. Kovarnik, C. W. Wang, H. C. Chen, T. P. Exarchos, D. I. Fotiadis, F. Destrempes, G. Cloutier, O. Pujol, M. Alberti, E. G. M. Ruiz, M. Rivera, T. Aksoy, R. W. Downe, and I. A. Kakadiaris, "Standardized evaluation methodology and reference database for evaluating Ivus Image segmentation", *Computerized Medical Imaging and Graphics*, Vol. 38, No. 2, pp. 70–90, 2014.

[26] Z. Gao, W. Guo, X. Liu, W. Huang, H. Zhang, N. Tan, W. K. Hau, Y. T. Zhang, and H. Liu, "Automated Detection Framework of the calcified plaque with acoustic shadowing in IVUS images", *PLoS One*, Vol. 9, No. 11, 2014.

[27] A. Taki, Z. Najafi, A. Roodaki, S. K. Setarehdan, R. A. Zoroofi, A. Konig, and N. Navab, "Automatic segmentation of calcified plaques and vessel borders in Ivus Images", *International Journal of Computer Assisted Radiology and Surgery*, Vol. 3, Nos. 3-4, pp. 347–354, 2008.